Check for updates

NANO · MICRO small
www.small-journal.com

Electrochemical Investigation of Calcium Substituted Monoclinic $Li_3V_2(PO_4)_3$ Negative Electrode Materials for Sodium- and Potassium-Ion Batteries

Qiang Fu, Bingrui Guo, Weibo Hua, Angelina Sarapulova, Lihua Zhu, Peter G. Weidler, Alexander Missyul, Michael Knapp, Helmut Ehrenberg, and Sonia Dsoke**

Herein, the electrochemical properties and reaction mechanism of $Li_{3-2x}Ca_xV_2(PO_4)_3$/C (x = 0, 0.5, 1, and 1.5) as negative electrode materials for sodium-ion/potassium-ion batteries (SIBs/PIBs) are investigated. All samples undergo a mixed contribution of diffusion-controlled and pseudocapacitive-type processes in SIBs and PIBs via Trasatti Differentiation Method, while the latter increases with Ca content increase. Among them, $Li_3V_2(PO_4)_3$/C exhibits the highest reversible capacity in SIBs and PIBs, while $Ca_{1.5}V_2(PO_4)_3$/C shows the best rate performance with a capacity retention of 46% at 20 C in SIBs and 47% at 10 C in PIBs. This study demonstrates that the specific capacity of this type of material in SIBs and PIBs does not increase with the Ca-content as previously observed in lithium-ion system, but the stability and performance at a high C-rate can be improved by replacing Li^+ with Ca^{2+}. This indicates that the insertion of different monovalent cations (Na^+/K^+) can strongly influence the redox reaction and structure evolution of the host materials, due to the larger ion size of Na^+ and K^+ and their different kinetic properties with respect to Li^+. Furthermore, the working mechanism of both LVP/C and $Ca_{1.5}V_2(PO_4)_3$/C in SIBs are elucidated via *in operando* synchrotron diffraction and *in operando* X-ray absorption spectroscopy.

1. Introduction

Recently, sodium-ion batteries (SIBs) and potassium-ion batteries (PIBs) have received much attention for large-scale energy storage to preserve lithium-ion batteries (LIBs) owing to their abundant resources and low cost as well as to the similar "rocking chair" working principle as in LIBs. Meanwhile, Aluminum can be used as the current collector in positive and negative electrodes for both SIBs and PIBs, whereas an expensive and heavier Cu foil must be used as a current collector in negative electrodes for LIBs, because of the Li–Al alloy formation at low potential.[1] Potassium-ion in propylene carbonate (PC) displays a lower ion-solvent interaction due to lower desolvation energy and a smaller solvated ion compared to Li- and Na-ion, resulting in fast diffusion kinetics and high rate capability.[2] However, due to the large ionic radius of Na^+ (1.02 Å) and K^+ (1.38 Å),[3] (which results in sluggish diffusion kinetics), SIBs and PIBs are still facing big challenges, such as sluggish diffusion kinetics in host structures.

Graphite is commonly used as negative electrode material for LIBs because of its flat and low working potential (0.1–0.2 V versus Li^+/Li) and relatively high specific capacity (372 mAh g^{-1}). Unfortunately, graphite is electrochemically less active in Na cells and cannot be used as an insertion host in SIBs since Na^+ insertion into graphite is significantly impeded,[4] while it is possible to co-intercalate Na-diglyme species.[5] This might be due to the unfavorable mismatch between the graphite structure and the size of

Q. Fu, B. Guo, W. Hua, A. Sarapulova, L. Zhu, M. Knapp, H. Ehrenberg, S. Dsoke
Institute for Applied Materials (IAM)
Karlsruhe Institute of Technology (KIT)
Hermann-von-Helmholtz-Platz 1,
D-76344 Eggenstein-Leopoldshafen, Germany
E-mail: qiang.fu@kit.edu; sonia.dsoke@kit.edu

W. Hua
School of Chemical Engineering and Technology
Xi'an Jiaotong University
Xi'an, Shaanxi 710049, P. R. China

P. G. Weidler
Institute of Functional Interfaces (IFG)
Chemistry of Oxidic and Organic Interfaces (COOI)
Karlsruhe Institute of Technology (KIT)
Hermann-von-Helmholtz-Platz 1, D-76344 Eggenstein-Leopoldshafen, Germany

A. Missyul
CELLS-ALBA Synchrotron
Cerdanyola del Valles, Barcelona E-08290, Spain

The ORCID identification number(s) for the author(s) of this article can be found under https://doi.org/10.1002/smll.202304102

© 2023 The Authors. Small published by Wiley-VCH GmbH. This is an open access article under the terms of the Creative Commons Attribution License, which permits use, distribution and reproduction in any medium, provided the original work is properly cited.

DOI: 10.1002/smll.202304102

the Na^+ ion and the energetic instability of the Na-graphite intercalation compounds.[6] Unlike the poor performance of graphite in SIBs, graphite can form KC_8 by K^+ ion intercalation with the high charge capacity of 273 mAh g^{-1} and good reversibility.[7] However, graphite also suffers from volume expansion and unsatisfactory cycling stabilities during potassium ion intercalation/deintercalation, which might cause safety issues and low Coulombic efficiency and hinder its practical application.[8] At present, hard carbon is considered the best option for SIBs and exhibits a low potential plateau ≤0.2 V (Na^+/Na) with a high capacity, delivering high power density in SIBs. Meanwhile, hard carbon delivers stable cycling performance in PIBs and is considered as a "reference" negative electrode material for SIBs due to its low cost, 3D structure, high specific capacity, and renewable resources.[9] Moreover, a large variety of hard carbon can be developed depending on the peculiar properties (porosity surface area, etc.).[9–10] Recently, the company CATL has launched commercial SIBs, consisting of a Prussian-white positive electrode and a hard carbon negative electrode with porous structure, where the battery provides a high energy density of 160 Wh kg^{-1} and fast charge to 80% state of charge (SOC) in 15 min.[11] Despite these progresses, it is necessary to develop other attractive negative electrode materials for SIBs and PIBs.

Recently, lithium vanadium phosphate $Li_3V_2(PO_4)_3$ (LVP) has attracted much attention as an electrode material for LIBs due to its excellent cycling stability, high thermal stability, and low synthetic cost.[12] Moreover, LVP has two different crystal structures: rhombohedral and monoclinic, with the space groups *R*-3 and $P2_1/n$, respectively. In the monoclinic phase, all three Li are mobile and are more facile to move in/out of the structure than in the rhombohedral one.[13] Besides, LVP can be employed as both positive and negative electrodes in LIBs due to its wide potential range.[12] However, pure LVP suffers from low intrinsic electronic conductivity, which may limit the application of this material in high-power devices.

To improve its electronic conductivity effectively, two strategies, including surface carbon coating and substitution of Li/V, are adopted.[12,14] Carbon sources are used as reducing agents to reduce V^{5+} to V^{3+} and to relieve aggregation/growing-up of LVP particles during synthesis. The substitution of Li/V with Ca^{2+} and Mg^{2+} can facilitate the Li^+ ion transport in the structure and improve the structure stability, cycling stability, and rate capability. For instance, the effect of Ca^{2+}-substituted LVP negative electrodes in LIBs was investigated by our group,[14a] who discovered that $Li_{3-2x}Ca_xV_2(PO_4)_3$/C compounds deliver specific capacities of 390, 274, 393, and 493 mAh g^{-1} at 1 C for x = 0, 0.5, 1, and 1.5, respectively. Despite the high polarization at 200 C, the electrodes deliver specific capacities higher than 50 mAh g^{-1}, indicating the high potential as promising negative electrode candidates for the realization of advanced high-power and energy devices. Our team[15] and other groups[16] reported $Na_3V_2(PO_4)_3$/C (NVP/C) negative electrodes for SIBs, which delivers a reversible capacity of 170 mAh g^{-1} at 20 mA g^{-1} in the potential range of 3.0–0.01 V versus Na^+/Na, corresponding to 3 Na^+ ions insertion/extraction. NVP/C exhibits long-cycle life with 62% capacity retention after 3000 cycles at 2 A g^{-1}. Zhang and coworkers[17] reported that NASICON-type $K_3V_2(PO_4)_3$ (KVP) delivers a reversible specific capacity of 130 and 91 mAh g^{-1} as both, negative and positive electrodes in the range of 2.5–1.0 V (negative electrode) and 2.0–4.0 V (positive electrode) for PIBs, respectively. Recently, we also reported a new pseudocapacitive $Mg_3V_4(PO_4)_6$/carbon negative electrode for Li/Na/K-ion batteries, which exhibits initial discharge/charge capacities of 961/607 mAh g^{-1} and capacity of over 547 mAh g^{-1} in the following five cycles for LIBs, much lower initial discharge/charge capacity of 236/63 and 301/64 mAh g^{-1} for SIBs and PIBs, respectively.[18]

By considering the above exciting results, we aim to extend the study of monoclinic LVP and Ca-substituted LVP as negative electrode materials for SIBs and PIBs and investigate the electrochemical properties of $Li_{3-2x}Ca_xV_2(PO_4)_3$/C (x = 0, 0.5, 1, and 1.5). Meanwhile, the insertion-type LVP-based materials possess low volume change during cycling and therefore have a high level of safety and stability. Furthermore, *in operando* synchrotron diffraction and *in operando* X-ray absorption spectroscopy (XAS) elucidated the working mechanism of both LVP/C and $Ca_{1.5}V_2(PO_4)_3$/C in SIBs.

2. Experimental Section

2.1. Synthesis of $Li_{3-2x}Ca_xV_2(PO_4)_3$/C

A series of materials $Li_{3-2x}Ca_xV_2(PO_4)_3$/C (x = 0, 0.5, 1, and 1.5) were synthesized by ball-milling (Planetary Micro Mill, PULVERISETTE 7, premium line, FRITSCH) and carbon-thermal reduction method. The same procedure can be found in our previous work,[14a] where a different type of ball-milling machine (Planetary Mono Mill PULVERISETTE 6 classic line, FRITSCH) was used.

2.2. Structural and Morphological Characterization

The carbon content in $Li_{3-2x}Ca_xV_2(PO_4)_3$/C (x = 0, 0.5, 1.0, and 1.5) was studied by thermo-gravimetric analysis (TGA) on STA 449C (Netzsch GmbH) under O_2 flow. The crystal structure of the materials was investigated using synchrotron radiation at the beamline P02.1 at DESY in Hamburg (λ = 0.20723 Å, 60 keV).[19] Powder samples were measured in a glass capillary (0.5 mm in diameter). The diffraction data were analyzed by the Rietveld method using the Fullprof software package.[20] The morphology of materials was studied with a Zeiss Supra 55 Scanning Electron Microscope (SEM). A LabRam Evolution HR from Horiba equipped with HeNe laser (633 nm, 17 mW) and a CCD detector (Horiba) was used to collect the Raman scattering of the samples. Meanwhile, a 600 grating was used to split the measurement signal with a ×50 objective (NA 0.95) for all the pristine and cycled samples. The data was collected for 30 s with 1.7 mW of the laser and five measurements were added to reduce the signal noise.

2.2.1. Specific Surface Area and Porosity

The Brunauer–Emmett–Teller method[21] was used to estimate the specific surface areas (SSA_{BET}) of $Li_{3-2x}Ca_xV_2(PO_4)_3$/C materials. The samples, average weight ≈135 mg, were outgassed overnight at 95 °C under a vacuum. During the outgassing process, ≈9% mass loss was recorded. The argon sorption was carried out with a Quantachrome Autosorb 1-MP (A.Paar, Austria)

© 2023 The Authors. Small published by Wiley-VCH GmbH

16136829, 0, Downloaded from https://onlinelibrary.wiley.com/doi/10.1002/smll.202304102 by Karlsruher Inst F. Technologie, Wiley Online Library on [17/07/2023]. See the Terms and Conditions (https://onlinelibrary.wiley.com/terms-and-conditions) on Wiley Online Library for rules of use; OA articles are governed by the applicable Creative Commons License

at 87.4K with 23 adsorption- and 6 desorption points. Ar provides better adsorption for the estimation of SSA because of its monatomicity and nonlocalization of the adsorbent during adsorption.[22] The pore size volume distribution, but also the specific surface area, denoted as SSA_{DFT}, were calculated with models based on DFT/Monte Carlo methods assuming a mixture of spherical and cylindrical pores on a carbon-based substrate.[23]

2.3. Electrochemical Characterization

The working electrode (active material, C65, and sodium-alginate binder in a ratio of 8:1:1) was prepared using the same procedure as in the previous paper,[14a] except for the current collector of Al-foil instead of Cu. The coated electrodes were cut into circular pieces with 12 mm diameter (1.131 cm^2, ≈2 mg cm^{-2}) and dried in the vacuum oven (Büchi Labortechnik GmbH) at 120 °C for at least 12 h to remove the moisture. The electrochemical performance of the negative electrode material was studied in 2-electrode Swagelok cells, where metallic sodium or potassium was used as a counter electrode with a GF/D Whatman separator. The electrolyte for SIBs was 1 M $NaClO_4$ in a mixture of ethylene carbonate (EC), propylene carbonate (PC) (1:1 by volume), and 2% (by volume) fluoroethylene carbonate (FEC). The electrolyte for PIBs was 1 M potassium bis(fluorosulfonyl)imide (KFSI) in a mixture of EC, diethyl carbonate (DEC) (1:1 by volume), or 1 M potassium hexafluorophosphate (KPF_6) dissolved in PC. Cyclic voltammetry (CV) and galvanostatic cycling with potential limitation (GCPL) were performed in the potential range of 3–0.01 V. The CV measurement was performed at different scan rates from 0.05 to 2 mVs^{-1}. All electrochemical measurements (CV and GCPL) were performed on a VMP3 multichannel potentiostat (Biologic Science Instrument) with the EC-lab software for instrument operation and data evaluation.

2.4. In Operando Synchrotron Diffraction and in Operando X-ray Absorption Spectroscopy (XAS)

In operando synchrotron diffraction was performed at Material Science and Powder Diffraction beamline (MSPD) at ALBA, Spain[24] and at PETRA-III beamline P02.1 at DESY in Hamburg, Germany.[19] The electrochemical cells consist of 2025-type coin cells with glass windows of 5 mm diameter for beam entrance. The negative electrode (active materials, ≈2.0 mg, and ≈7 mg cm^{-2}) was prepared by pressing the electrode mixture on Al mesh within a 5 mm hole in the center. Preliminary *in operando* synchrotron diffraction was conducted at ALBA with radiation wavelength λ = 0.41273 Å (30 keV), and position sensitive detector MYTHEN, where data were collected with an effective exposure time of 60 s in steps of 0.006° over the angular range of 1.8°–42° in 2theta during the first cycles at C/11 for SIBs. *In operando* synchrotron diffraction was conducted at DESY/PETRA-III at beamline P02.1 with radiation wavelength λ = 0.20695 Å (60 keV), where data were collected with an effective exposure time of 40 s during the first cycles at C/11 (LVP/C) and C/13 ($Ca_{1.5}V_2(PO_4)_3$/C) for SIBs. DAWN software is used to process the 2D powder diffraction.[25] The diffraction data analysis was carried out by the Rietveld method using the Fullprof software package.[20] *In operando* X-ray absorption spectroscopy (XAS) measurements were carried out at PETRA-III beamline P64 at DESY in Hamburg during the first cycle at C/11 (LVP/C) and C/13 ($Ca_{1.5}V_2(PO_4)_3$/C) for SIBs between 3 V and 0.01 V. XAS spectra were recorded in quick-XAS (5 min per spectrum) mode in fluorescence geometry using a PIPS diode. The V K-edge of LVP/C and $Ca_{1.5}V_2(PO_4)_3$/C was measured during the electrochemical cycling and the energy was calibrated using the absorption edge of V foil, as it is commonly employed in XAS experiments. All data were collected at room temperature with a Si (111) double crystal monochromator and all XAS spectra were processed using DEMETER software package.[26]

3. Results and Discussion

3.1. Structural and Morphological Characterization

The phase purity and crystal structure of the as-prepared samples were characterized by synchrotron diffraction and shown in Figure S1, Supporting Information. All synchrotron diffraction patterns show intense and sharp reflections, indicating a good crystallinity of $Li_{3-2x}Ca_xV_2(PO_4)_3$/C materials. The Rietveld method was performed to analyze their structure and their lattice parameters, given in Tables S1–S5, Supporting Information, are in agreement with our previous work.[14a] Briefly, all featured diffraction reflections observed for the pristine $Li_3V_2(PO_4)_3$/C can be well indexed to monoclinic $Li_3V_2(PO_4)_3$ with a space group of $P2_1/n$. On the other hand, the fully substituted material $Ca_{1.5}V_2(PO_4)_3$/C has a rhombohedral structure with the space group R-3c, including an impurity of 5% $Ca_3(PO_4)_2$. $Li_2Ca_{0.5}V_2(PO_4)_3$/C and $LiCaV_2(PO_4)_3$/C are mixtures of monoclinic $Li_3V_2(PO_4)_3$ and rhombohedral $Ca_{1.5}V_2(PO_4)_3$. Scanning electron microscopy (SEM) (Figure S2, Supporting Information) displays that all composites are made of densely packed agglomerates and the particle sizes are estimated to be 100–700 nm, with no big differences from our previous work.[14a] TGA demonstrates the presence of carbon in the composites with an amount of 5.2, 4.6, 3.9, and 4.2 wt.%, for $Li_{3-2x}Ca_xV_2(PO_4)_3$/C (x = 0, 0.5, 1.0, and 1.5, respectively) (Figure S3, Supporting Information). These results have a deviation of ≈2% from our previous work,[14a] which might be attributed to the different ball-milling equipment and tube furnace as well as the faster gas flow. Raman scattering (Figure S4, Supporting Information) shows several peaks at ≈301.2, 428.2, 974.1, 1062.6, 1339 (D band), and 1590 cm^{-1} (G band), where the two broad D and G bands agree with our previous work.[14a] Two peaks at 974.1 and 1062.6 cm^{-1} are assigned to PO_4 valence bond vibrations and the peak at 428.2 cm^{-1} comes from PO_4 deformation vibration, while the one at 301.2 cm^{-1} is from external lattice vibration.[27] Interestingly, PO_4 valency bond vibration at 974.1 cm^{-1} continuously shifts to lower Raman shift (951 cm^{-1} for $Ca_{1.5}V_2(PO_4)_3$/C) with increasing Ca substitution, while the external lattice vibration at 301.2 cm^{-1} continuously shifts to higher Raman shift (314.9 cm^{-1} for $Ca_{1.5}V_2(PO_4)_3$/C). The surface area of LVP/C is 59 m^2 g^{-1}, while the one of $Ca_{1.5}$VP/C is only 23 m^2 g^{-1}, in good agreement with our previous work.[14a] The two intermediate compositions $Li_2Ca_{0.5}V_2(PO_4)_3$/C and $LiCaV_2(PO_4)_3$/C have surface areas of 47 and 26 m^2 g^{-1}, respectively, deviation of ≈15 m^2 g^{-1} from previous work (Figure S5, Supporting Information).

© 2023 The Authors. Small published by Wiley-VCH GmbH

16136829, 0, Downloaded from https://onlinelibrary.wiley.com/doi/10.1002/smll.202304102 by Karlsruher Inst F. Technologie, Wiley Online Library on [17/07/2023]. See the Terms and Conditions (https://onlinelibrary.wiley.com/terms-and-conditions) on Wiley Online Library for rules of use; OA articles are governed by the applicable Creative Commons License

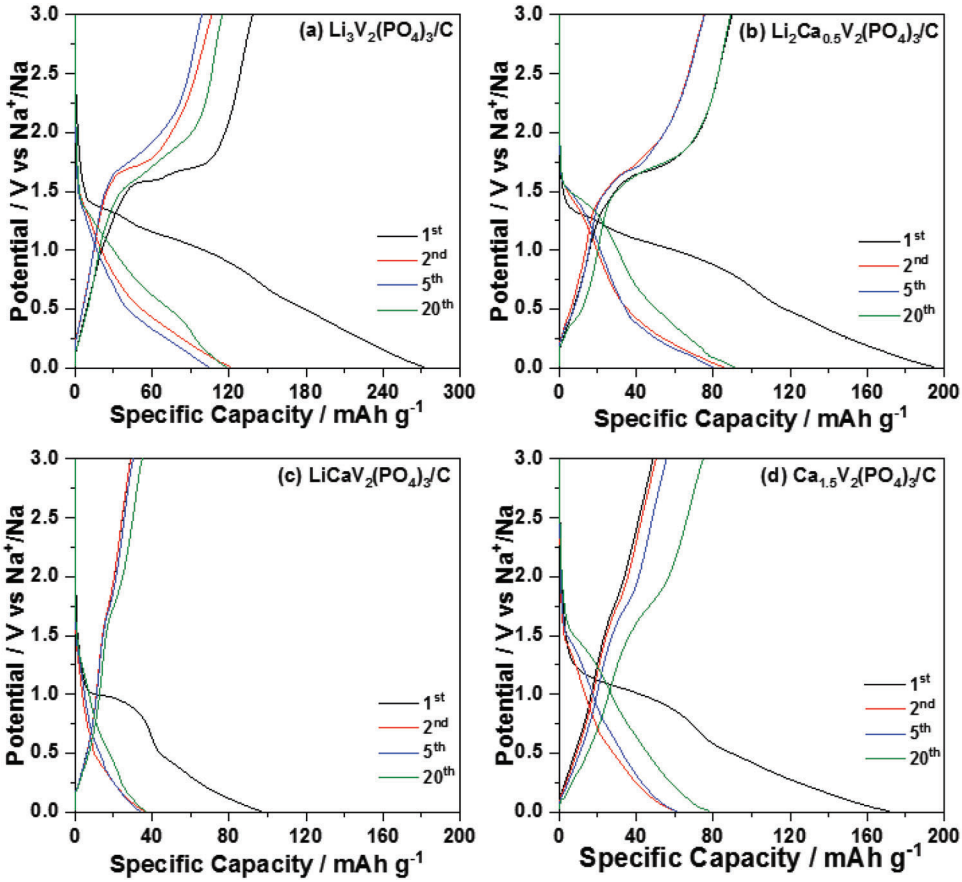

Figure 1. The charge-discharge curves of $Li_3V_2(PO_4)_3$/C (a), $Li_2Ca_{0.5}V_2(PO_4)_3$/C (b), $LiCaV_2(PO_4)_3$/C (c), and $Ca_{1.5}V_2(PO_4)_3$/C (d) at 0.1 C at 25 °C for Na-based half cells.

3.2. Electrochemical Properties in SIBs

The electrochemical activity of $Li_{3-2x}Ca_xV_2(PO_4)_3$/C negative electrodes in Na-based half cells was studied by galvanostatic cycling in the potential range of 3.0–0.01 V versus Na^+/Na at C/10 at 25 °C (**Figure 1**). Note that 1 C refers to the theoretical capacity calculated considering 4 Na^+ ions insertion for all samples similar to that reported for LIBs.[14a]

LVP/C material (Figure 1a) displays a slope with three steps during the 1st discharge (sodiation process). Meanwhile, two short plateaus at 1.59 and 1.69 V followed by one slope are observed during the 1st charge (desodiation process). Only a slope-like curve can be observed during the following discharge processes while the charge profiles are analogous to each other, with a voltage plateau at ≈1.7 V from the second cycle. LVP/C material offers initial sodiation and desodiation capacities of 272 and 138 mAh g^{-1} (≈2 Na^+ reversibly inserted), respectively (Table S6, Supporting Information), resulting in an initial irreversible capacity loss (134 mAh g^{-1}). This largely irreversible capacity loss could be related to the formation of a solid electrolyte interface (SEI) layer and the decomposition of the electrolyte, which is commonly occurring at such low potential and is very similar to LIBs.[16] In the 2nd cycle, the sodiation and desodiation capacities are 121 and 107 mAh g^{-1}, respectively, giving a reduced irreversible capacity loss (14 mAh g^{-1}). After the 5th cycle, the specific capacity starts to increase and stabilizes at ≈131 mAh g^{-1} after 200 cycles with almost 100% coulombic efficiency, as shown in **Figure 2**. Compared with LVP/C, $Li_2Ca_{0.5}V_2(PO_4)_3$/C (Figure 1b) exhibits similar discharge and charge profiles. It shows initial

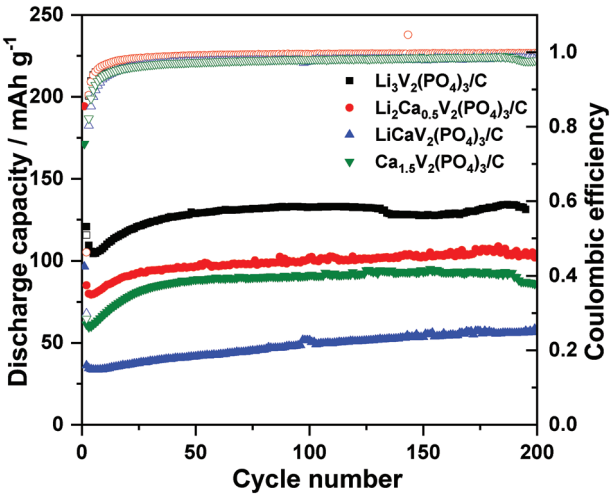

Figure 2. Cycle performance and coulombic efficiency of $Li_{3-2x}Ca_xV_2(PO_4)_3$/C at 0.1 C for Na-based half cells.

© 2023 The Authors. Small published by Wiley-VCH GmbH

16136829, 0, Downloaded from https://onlinelibrary.wiley.com/doi/10.1002/smll.202304102 by Karlsruher Inst F. Technologie, Wiley Online Library on [17/07/2023]. See the Terms and Conditions (https://onlinelibrary.wiley.com/terms-and-conditions) on Wiley Online Library for rules of use; OA articles are governed by the applicable Creative Commons License

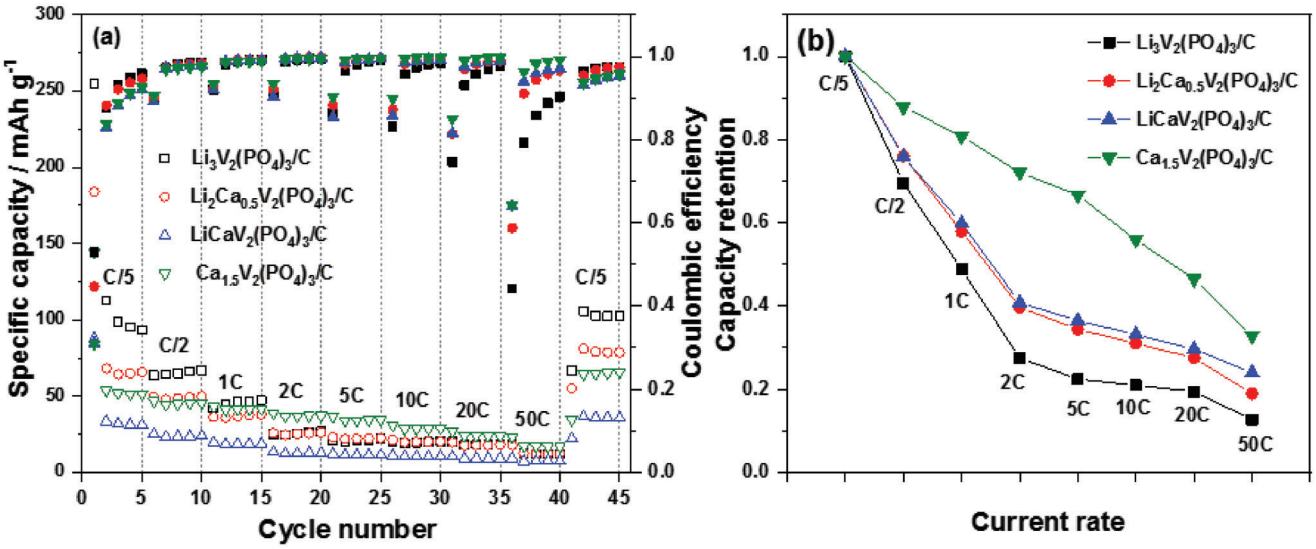

Figure 3. a) Specific capacities at increasing C-rates of $Li_{3-2x}Ca_xV_2(PO_4)_3$/C electrodes and b) capacity retention of $Li_{3-2x}Ca_xV_2(PO_4)_3$/C electrodes at increasing C-rates.

sodiation and desodiation capacities of 194 and 90 mAh g^{-1}, respectively, with an initial irreversible capacity loss of 104 mAh g^{-1}. In the 2nd cycle, the discharge capacity quickly drops to 85 mAh g^{-1} and stabilizes ≈101 mAh g^{-1} after 200 cycles (Figure 2). Both $LiCaV_2(PO_4)_3$/C and $Ca_{1.5}V_2(PO_4)_3$/C (Figure 1c-d) display two slope-like plateaus during the 1st discharge and 1st charge, which is different from what was observed in LVP/C. No clear plateaus can be observed in the following cycles. $LiCaV_2(PO_4)_3$/C (Figure 1c) only delivers initial sodiation and desodiation capacities of 97 and 29 mAh g^{-1}, respectively, with an irreversible capacity loss of 68 mAh g^{-1}. After the 5th cycle, the specific capacity increases and stabilizes at ≈51 mAh g^{-1} after 200 cycles (Figure 2). $Ca_{1.5}V_2(PO_4)_3$/C (in Figure 1d) delivers a sodiation capacity of 171 mA h g^{-1} and a reversible capacity of 49 mA h g^{-1} with an initial irreversible capacity loss of 123 mAh g^{-1}. After the 3rd cycle, its specific capacity increases and stabilizes at ≈91 mAh g^{-1} after 200 cycles (Figure 2).

Among the four samples, $Li_3V_2(PO_4)_3$/C displays the highest reversible sodiation capacity of 132 mAh g^{-1} after 200 cycles. Unfortunately, these values are still rather low, as compared with that of NVP (150 mAh g^{-1})[16,28] and less than half of the capacity of hard carbon (300 mAh g^{-1}),[10b] while the $LiCaV_2(PO_4)_3$/C displays the lowest capacity. Although the initial coulombic efficiency is very low for all samples, it tends to stabilize at ≈99% at the 15th cycle, which could be attributed to an activation process due to the large size of Na^+ during Na^+ insertion/deinsertion.

Furthermore, the rate capability of $Li_{3-2x}Ca_xV_2(PO_4)_3$/C was investigated in the C-rate range from 0.2 to 50 C despite their poor capacities, as shown in **Figure 3**. Among the four samples, $Li_3V_2(PO_4)_3$/C provides the highest specific sodiation capacity at C-rates lower than 1C, while $LiCaV_2(PO_4)_3$/C shows the lowest one. With further increasing C-rates, $Ca_{1.5}V_2(PO_4)_3$/C and $LiCaV_2(PO_4)_3$/C show the highest and lowest specific sodiation capacity, respectively, while LVP/C and $Li_2Ca_{0.5}V_2(PO_4)_3$ have similar capacities, which lie in between. $Ca_{1.5}V_2(PO_4)_3$/C delivers specific capacities higher than 15 mAh g^{-1} at 50 C, while it shows specific capacities higher than 50 mAh g^{-1} at 200C in LIBs.[14a] 50 C is a quite high C-rate for SIB materials, and most negative electrode materials in SIBs do not afford such a high C-rate except few negative electrode materials like $Na_2Ti_3O_7$/C (mass loading of 1.5–2.0 mg cm^{-2}), Anatase TiO_2 (mass loading of 3.5 mg cm^{-2}), P-doped carbon nanosheets, and hard carbon (mass loading of 1.0 mg cm^{-2}, only few works reported hard carbon at such high C rate).[29] Note that cathode materials often show a much better rate of performance than anode for SIBs.[30] In addition, it could be a good approach to figure out the reasons behind the differences in the rate performance of different materials. However, it is much more complicated than that of the NVP cathode[30b] due to the SEI formation and strong side reaction in both SIBs and PIBs and will be a follow-up work in the future.

Figure 3b exhibits the capacity retention of the $Li_{3-2x}Ca_xV_2(PO_4)_3$/C. LVP/C displays poor capacity retention with an increasing current rate. All the substituted samples demonstrate higher capacity retention than that LVP/C. At 20 C, $Ca_{1.5}V_2(PO_4)_3$/C has a capacity retention of 46%. Although LVP/C shows the highest specific sodiation capacity until 1 C, its capacity retention at higher C-rates rates is only ≈20%. In summary, $Ca_{1.5}V_2(PO_4)_3$/C displays superior rate performance in SIBs compared with the other three materials, whereas it also shows superior rate performance in LIBs.

The electrochemical behavior of $Li_{3-2x}Ca_xV_2(PO_4)_3$/C electrodes was studied by cyclic voltammetry (CV) at a scan rate of 0.05 mV s^{-1} versus Na^+/Na between 3 and 0.01 V as shown in **Figure 4**. All four samples display two broad reduction peaks at ≈0.45 and 1.0 V and one broad oxidation peak at ≈1.7–1.8 V. The two reduction peaks are related to the formation of the solid electrolyte interphase (SEI) film caused by the decomposition of the electrolyte and disappear in the subsequent cycles. In the first scan of the LVP/C electrode, one more reduction peak located at 1.26 V and two nearly overlapped oxidation peaks at 1.68 and 1.74 V are observed (also in agreement with dQ/dE plot Figure S6, Supporting Information). In the following scans, both two oxidation peaks tend to merge into one broader peak.

© 2023 The Authors. Small published by Wiley-VCH GmbH

16136829, 0, Downloaded from https://onlinelibrary.wiley.com/doi/10.1002/smll.202304102 by Karlsruher Inst F. Technologie, Wiley Online Library on [17/07/2023]. See the Terms and Conditions (https://onlinelibrary.wiley.com/terms-and-conditions) on Wiley Online Library for rules of use; OA articles are governed by the applicable Creative Commons License

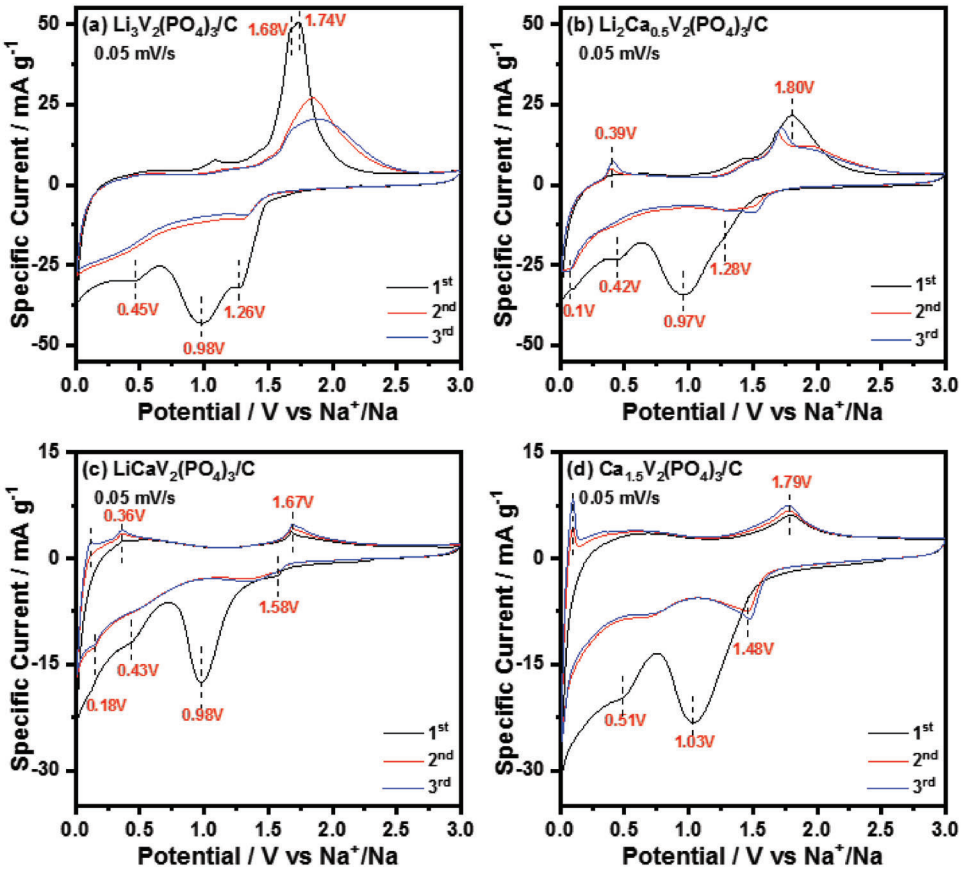

Figure 4. CV curves of $Li_3V_2(PO_4)_3$/C (a), $Li_2Ca_{0.5}V_2(PO_4)_3$/C (b), $LiCaV_2(PO_4)_3$/C (c), and $Ca_{1.5}V_2(PO_4)_3$/C (d) at scan rates of 0.05 mV s^{-1} in the potential range of 3.0–0.01 V vs. Na^+/Na.

The merging and broadening of the peaks might be caused by the increased polarization. In the subsequent cycles, a pair of redox peaks between 1.2 and 1.8 V corresponds to the reversible reduction of V^{3+} to V^{2+}, consistent with previous reports with $Na_3V_2(PO_4)_3$.[16,31] $Li_2Ca_{0.5}V_2(PO_4)_3$/C and $LiCaV_2(PO_4)_3$/C show similar redox peaks compared with $Li_3V_2(PO_4)_3$/C. After the first cycle, another reduction peak at 0.1 V and an oxidation peak at ≈0.4 V appear, which implies a further reduction and oxidation processes of vanadium[13]. The material shows one pair of redox peaks at 1.52 V/1.72 V and nearly overlapped CV curves in the following scans. $Ca_{1.5}V_2(PO_4)_3$/C exhibits one pair of redox peaks at 1.5/1.8 V after the second scan. Also at the low working potential (nearly 0 V), a pair of redox peaks centered at 0.09 V appears starting from the 2nd cycle. Notably, all CV profiles from the 2nd cycle are nearly overlapping with the 3rd scan, suggesting good electrochemical reversibility.

Differential capacity plots (dQ/dE) (Figure S6, Supporting Information) of $Li_{3-2x}Ca_xV_2(PO_4)_3$/C materials calculated from discharge-charge profiles at 0.1 C demonstrate that these peaks are sharper, distinct, and consistent with the CV curves. Along with increasing the Ca content, both CV curves and dQ/dE plots show a similar trend: during the first discharge cycle, the reduction peaks change from three to two. The two reduction peaks in the potential range of 0.9 V – 1.4 V are merged into one broad peak. All the Ca-substituted samples display an oxidation peak in the low potential region ≈0.5 V, which becomes more and more evident as the calcium content increases.

Cyclic voltammetry was further performed at different scan rates (from 0.05 to 2 mV s^{-1}) to analyze the reaction kinetics (Figure S7, Supporting Information). With the increase in scan rate, LVP/C shows a dramatically increasing and broadening ladder-shaped oxidation peak, while the other three samples exhibit shifts to lower/higher potentials for reduction/oxidation peaks. Additionally, $Ca_{1.5}V_2(PO_4)_3$/C also displays an increase in current of the redox peak 0.1/0.5 V. Along with increasing the Ca content, the capacity contribution due to the oxidation reaction below 1.5 V increases (Figure S7c-d, Supporting Information). Compared with that of LVP/C in the low potential range, CV of $Ca_{1.5}V_2(PO_4)_3$/C has less deformation at high current, indicating its lower resistance and meaning that $Ca_{1.5}V_2(PO_4)_3$/C can be applied to high-power devices. It is well known that activated carbon has excellent retention, but it cannot be used at such low potentials because of the very high surface area, which can trigger massive electrolyte decomposition and blockage of the pores. Note that most hard carbon electrode materials are not supported to run at such a high C rate up to 50 C.[29] For instance, P-doped carbon nanosheets deliver a capacity of 108 mAh g^{-1} even at 20 A g^{-1} (unfortunately, no mass loading was provided by the authors)[29d] and hard carbon (mass loading of 1.0 mg cm^{-2}) offers a capacity of 214 mAh g^{-1} at 10 A g^{-1} in ether electrolytes.[29e]

© 2023 The Authors. Small published by Wiley-VCH GmbH

16136829, 0, Downloaded from https://onlinelibrary.wiley.com/doi/10.1002/smll.202304102 by Karlsruher Inst F. Technologie, Wiley Online Library on [17/07/2023]. See the Terms and Conditions (https://onlinelibrary.wiley.com/terms-and-conditions) on Wiley Online Library for rules of use; OA articles are governed by the applicable Creative Commons License

These results further demonstrate that $Ca_{1.5}V_2(PO_4)_3/C$ can be applied to high-power devices such as hybrid supercapacitors.

It is well known that two extreme types of behavior can exist in electrochemical energy-storage devices when charged/discharged under constant current. The first one is related to battery type and most often results in a flat discharge plateau. The second one is attributed to capacitive type and exhibits a triangular-shaped plot during cycling. Intermediate behavior can be found when a faradaic electrode exhibits a sloped discharge curve due to the presence of surface-like processes.[32] In order to further analyze the electrochemical behavior, the specific voltammetric charge q was analyzed by the Trasatti Differentiation Method. It can be defined as[33]:

$$q = q_{\mathrm{i}} + q_{\mathrm{o}} \tag{1}$$

where q_i and q_o are the charges related to the "inner surface" and "outer surface", respectively.

The specific voltammetric charge q is estimated from each cyclic voltammogram at different scan rates based on the following equations:

$$q = S/2\, vm \tag{2}$$

$$S = \int_{U2}^{U1} I \mathrm{d}U \tag{3}$$

where v, m, and S are scan rate (V s^{-1}), mass (g) of active material, and graphical integrator directly on the recorded CV curves (A g^{-1} versus V).

Based on the Cottrell Equation:

$$q(v) \propto v^{-1/2} \tag{4}$$

q is linearly related to v. When v gradually increases, it may show an ohmic drop due to intrinsic resistance.

The q values calculated by Equations (2) and (3) can be plotted versus an appropriate function of the scan rate v, with the aim to extrapolate the values of q to $v = 0$ and ∞, respectively. When v approaches $+\infty$, i.e., just allows surface (electrode/electrolyte interfaces) processes to happen (Figure S8, Supporting Information):

$$q(v) = \frac{Const.}{\sqrt{v}} + q_o \tag{5}$$

where q_o is the contribution of the surface-controlled process.

When the scan rate v approaches 0, i.e., giving sufficient time for ions to diffuse and react (Figure S9, Supporting Information):

$$q(v) = \mathrm{Const.}\sqrt{v} + \frac{1}{q_t} \tag{6}$$

where q_t is the maximum total specific voltammetric capacity. The specific diffusion-controlled q_i can be obtained from the difference between q_t and q_o. **Table 1** summarizes q_t, q_i, q_o, and the ratio of pseudocapacitive contribution. For $Li_3V_2(PO_4)_3/C$, 40% of total specific capacity comes from pseudocapacitive capacity, indicating that a diffusion-controlled process dominates the electrochemical reaction of $Li_3V_2(PO_4)_3/C$. With the increase of Ca substitution, the contribution of the surface-controlled process gradually increases to 43%, 57%, and 88%, indicating that a pseudocapacitive process dominates the charge storage of $Ca_{1.5}V_2(PO_4)_3/C$. Note that the power-law relationship[34] of $i = av^b$ is not suitable to calculate the b value and to evaluate the diffusion-controlled and pseudo-capacitance contributions since log(i) versus log(v) plots of oxidation/reduction peaks do not fit a linear relationship.

Table 1. Summary of maximum total voltammetric capacity (q_t), diffusion-controlled capacity (q_i), and pseudocapacitive capacity (q_o) from the plots of q versus $v^{-1/2}$ and q versus $v^{1/2}$ for SIBs..

Sample	q_t (C g^{-1})	q_o (C g^{-1})	q_i (C g^{-1})	$q_{0/}\, q_t$ (%)
$Li_3V_2(PO_4)_3/C$	538	213	325	40
$Li_2Ca_{0.5}V_2(PO_4)_3/C$	353	150	203	43
$LiCaV_2(PO_4)_3/C$	190	108	82	57
$Ca_{1.5}V_2(PO_4)_3/C$	258	228	30	88

3.3. Electrochemical Properties in PIBs

[$Li_{3-2x}Ca_xV_2(PO_4)_3/C$ || 1 M KFSI in (EC/DEC) || K] and [$Li_{3-2x}Ca_xV_2(PO_4)_3/C$ || 1 M KPF_6 in (EC/PC) || K] cells were assembled to investigate the electrochemical performance of a $Li_{3-2x}Ca_xV_2(PO_4)_3/C$ negative electrode in PIBs (Figures S10–S11, Supporting Information). The potassiation and depotassiation capacities of materials in both K-based electrolytes are listed in Table S7–S8, Supporting Information.

All charge-discharge profiles show a slope-like shape. LVP/C delivers an initial potassiation and depotassiation capacity of 252 and 116 mAh g^{-1}, resulting in an initial irreversible capacity loss of 136 mAh g^{-1}. Note that the reversible capacity of LVP is comparable with some of the reported negative electrode materials for PIBs, such as $KTi_2(PO_4)_3$, $K_2Ti_8O_{17}$, $K_2Ti_4O_9$, and KVP,[35] whereas, unluckily, its reversible capacity is much lower than the most common graphite negative electrode with a capacity of ≈300 mAh g^{-1} in PIBs.[7] In contrast, $Li_2Ca_{0.5}V_2(PO_4)_3/C$ displays an initial potassiation and depotassiation capacity of 185 and 69 mAh g^{-1}, respectively, with an initial irreversible capacity loss of 116 mAh g^{-1}. In the second cycle, the discharge capacity quickly drops to 66 mAh g^{-1} and stabilizes at ≈45 mAh g^{-1} in the following cycles.

$LiCaV_2(PO_4)_3/C$ shows the lowest potassiation/depotassiation capacities of 76/25 mAh g^{-1} with an initial irreversible capacity loss of 51 mAh g^{-1}. After the 5th cycle, the specific capacity stabilizes at ≈22 mAh g^{-1}. Unfortunately, the low capacity of $LiCaV_2(PO_4)_3/C$ is far too low for a possible application of this material in PIBs. $Ca_{1.5}V_2(PO_4)_3/C$ delivers a discharge capacity of 149 mA h g^{-1} and a reversible capacity of 50 mA h g^{-1} with an initial irreversible capacity loss of 99 mAh g^{-1}. After several cycles, the specific capacity stabilizes at ≈55 mAh g^{-1}. Those values are much lower than those obtained in SIBs for the same material, respectively, implying better kinetics in SIBs due to the relatively smaller radius of Na^+ compared with K^+.

Figure S11, Supporting Information, displays the galvanostatic charge-discharge cycling of $Li_{3-2x}Ca_xV_2(PO_4)_3/C$ electrode with electrolyte KPF_6 over the potential range of 3.0–0.01 V versus

© 2023 The Authors. Small published by Wiley-VCH GmbH

16136829, 0, Downloaded from https://onlinelibrary.wiley.com/doi/10.1002/smll.202304102 by Karlsruher Inst F. Technologie, Wiley Online Library on [17/07/2023]. See the Terms and Conditions (https://onlinelibrary.wiley.com/terms-and-conditions) on Wiley Online Library for rules of use; OA articles are governed by the applicable Creative Commons License

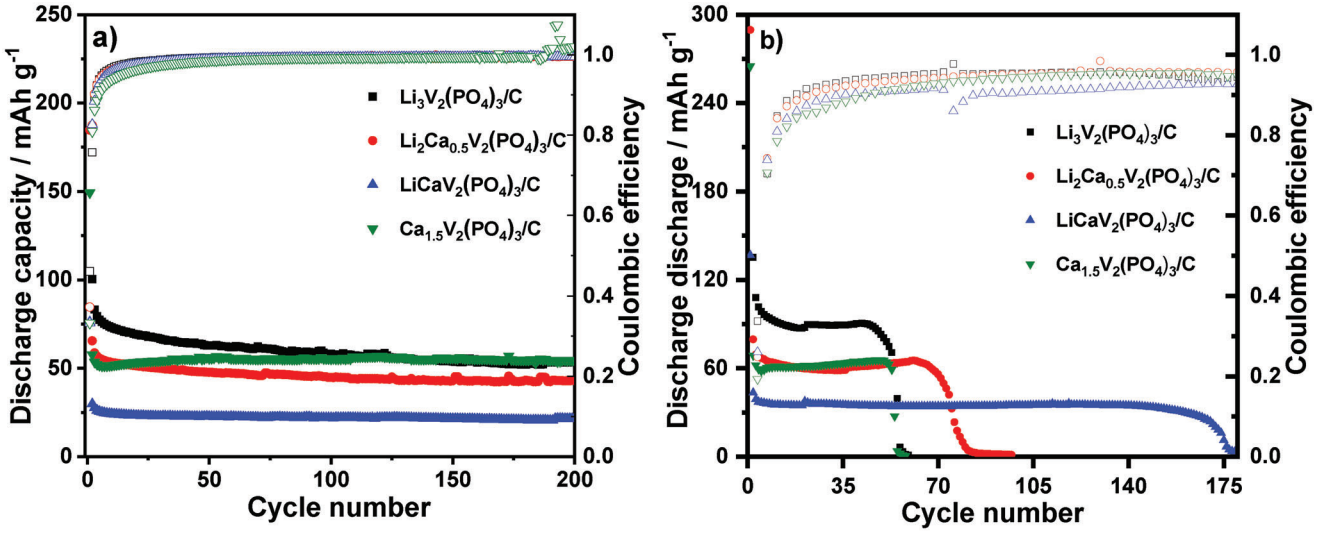

Figure 5. The cycle performance and coulombic efficiency of $Li_{3-2x}Ca_xV_2(PO_4)_3/C$ at 0.2 C at 25 °C in: a) KFSI-based electrolyte and b) KPF_6-based electrolyte.

K^+/K at 0.2 C. In comparison to the PIBs with KFSI (Figure S10, Supporting Information), no significant change in the charge-discharge curves is observed. Among the four materials, LVP/C possesses the highest reversible capacity, while $LiCaV_2(PO_4)_3/C$ has the lowest one. Interestingly, all $Li_{3-2x}Ca_xV_2(PO_4)_3/C$ materials in KPF_6-based electrolyte have higher capacity (70–100 mAh g^{-1}) than that in the KFSI-based one. Meanwhile, higher capacities of 15–30 mAh g^{-1} are obtained in the subsequent cycles. The reason for this phenomenon may be due to the decomposition of KPF_6-based electrolyte[36] (probably some extra capacity is reversible) while the KFSI-based one is more stable at low voltage.[37] In the subsequent cycles, the SEI layer formed in the KFSI-based electrolyte is stable; therefore, the capacity difference is reduced. Note that problems may arise when Na/K metal is used in half-cell experiments because of the highly reactive Na/K metal and side reaction of electrode/K metal,[38] where the decomposition products may affect the active material.

Figure 5 shows the cycling performance and coulombic efficiency of $Li_{3-2x}Ca_xV_2(PO_4)_3/C$ at 0.2 C in KFSI- and KPF_6-based electrolytes. All samples cycled in the KFSI-based electrolyte show a more stable cycling performance than those in KPF_6-based electrolytes. The coulombic efficiency of all samples in KFSI-based electrolytes is near 100% after several cycles, while the coulombic efficiency in the KPF_6-based electrolyte is ≈96%. Furthermore, the KPF_6-based electrolyte shows instability because the capacities drop abruptly after 50 cycles. Electrolytes are playing a critical role in the electrochemical performance of materials. For example, Wang et al.[37b] reported the impacts of the electrolyte salt and solvent chemistry on the stability of both K metal and amorphous red phosphorus (RP) electrodes in PIBs. It shows that organic components dominate the SEI layer when using 0.8 M KPF_6/EC+DEC, while more inorganic salts are generated when utilizing 1 M KFSI/EC+DEC. Compared to organic species, inorganic salts possess better mechanical strength to accommodate large volume changes. Moreover, 1 M KFSI/EC+DEC can effectively suppress K dendrite growth and inhibit electrolyte decomposition to boost the cycling and rate performance of K metal batteries.[37b] In KPF_6/PC, the capacities sharply decrease after ≈50 cycles, which might be attributed to the strong side reaction caused by K metal and electrolyte consumption.

Rate capability tests were performed using the KFSI-based electrolyte. Figure S12a, Supporting Information, provides the specific capacities delivered at increasing C-rates, ranging from 0.2 to 50 C. Among the four samples, $Li_3V_2(PO_4)_3/C$ material delivers the highest specific potassiation capacity up to 5 C, while the $LiCaV_2(PO_4)_3/C$ shows the lowest one. Moreover, $Li_3V_2(PO_4)_3/C$ material still delivers a reversible capacity of ≈50 mAh g^{-1} at 2 C. For C-rates higher than 5 C, the discharge capacities of all samples reach a minimum and are close to each other. $Ca_{1.5}V_2(PO_4)_3/C$ shows the best capacity retention at increasing C-rates (Figure S12b, Supporting Information). All the substituted samples demonstrate higher capacity retention than that of LVP/C, being promising materials for high-power devices. At 10 C, $Ca_{1.5}V_2(PO_4)_3/C$ still has a capacity retention of 47%. Although LVP/C shows the highest specific potassiation capacity up to 5 C, the capacity retention at higher C-rates is not ideal, with only ≈28% of retention.

Figure 6 shows the CV profiles of the four $Li_{3-2x}Ca_xV_2(PO_4)_3/C$ electrodes in KFSI-based electrolyte recorded at a scan rate of 0.05 mV s^{-1}. For all samples, an irreversible peak at ≈0.5 V is observed in CV curves, corresponding to the formation of SEI. $Li_3V_2(PO_4)_3/C$ shows three broad peaks at ≈0.46, 1.88, and 2.86 V in the first oxidation process. In the subsequent scans, no clear redox pair of peaks can be observed. $Ca_{1.5}V_2(PO_4)_3/C$ shows two reversible peaks at 0.50 and 1.95 V in the initial oxidation process.

Cyclic voltammetry was further performed at different scan rates (from 0.05 to 2 mV s^{-1}) to analyze the reaction kinetics (Figure S13, Supporting Information). With the increase of the scan rate, LVP/C shows a broad oxidation peak, while $Li_2Ca_{0.5}V_2(PO_4)_3/C$ and $LiCaV_2(PO_4)_3/C$ exhibit a broad peak at ≈1.2 V. The CV curves of $Ca_{1.5}V_2(PO_4)_3/C$ still show broad peaks,

© 2023 The Authors. Small published by Wiley-VCH GmbH

16136829, 0, Downloaded from https://onlinelibrary.wiley.com/doi/10.1002/smll.202304102 by Karlsruher Inst F. Technologie, Wiley Online Library on [17/07/2023]. See the Terms and Conditions (https://onlinelibrary.wiley.com/terms-and-conditions) on Wiley Online Library for rules of use; OA articles are governed by the applicable Creative Commons License

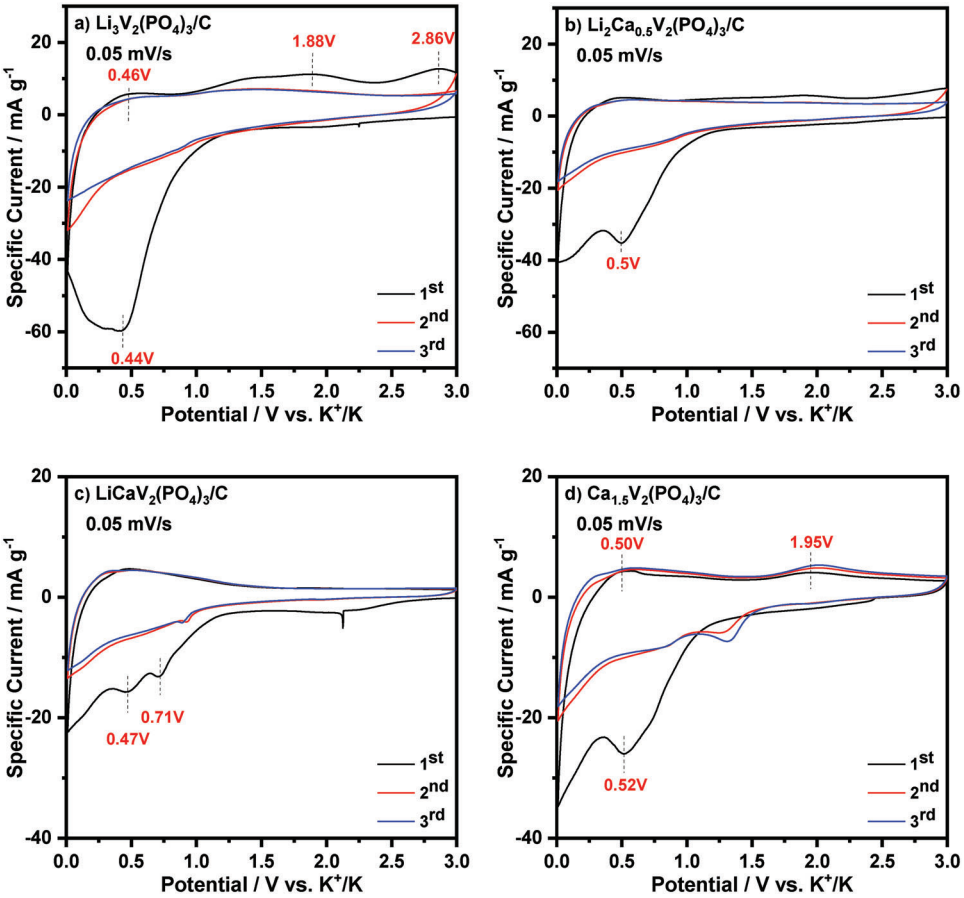

Figure 6. The CV profiles of $Li_3V_2(PO_4)_3$/C (a), $Li_2Ca_{0.5}V_2(PO_4)_3$/C (b), $LiCaV_2(PO_4)_3$/C (c), and $Ca_{1.5}V_2(PO_4)_3$/C (d) electrodes in KFSI-based electrolyte at scan rates of 0.05 mV s^{-1} in a potential range of 3.0 to 0.01 V vs. K^+/K.

but the reduction peak at ≈1 V is more defined with respect to the other materials. In contrast, KVP exhibits four pairs of distinct peaks in the 2.5–1.0 V range when used as an negative electrode in PIBs.[35d] Furthermore, the capacity contribution in the low-potential region increases along with the increasing scan rate. Among all samples, $Ca_{1.5}V_2(PO_4)_3$/C presents the highest current responses at high scan rates, suggesting that it can be applied to high-power hybrid capacitors.

The Trasatti Differentiation Method was applied to further analyze the electrochemical behavior, the specific voltammetric charge q. In the partition procedure, the total specific voltammetric charge q_t is given from the extrapolation of voltammetric charge q to $v = 0$ from the plot of q^{-1} versus $v^{1/2}$ (Figure S15, Supporting Information). The diffusion-controlled charge q_i is estimated from the extrapolation of q to $v = \infty$, from the plot of q versus $v^{-1/2}$ (Figure S14, Supporting Information). Accordingly, the surface-related contribution charge q_o can be obtained from the difference between q_t and q_i, (Table S9, Supporting Information).

For $Li_3V_2(PO_4)_3$/C, only 6.5% of the total specific capacity comes from the surface-related contribution process, indicating the predominance of a diffusion-controlled process in $Li_3V_2(PO_4)_3$/C. With the increase of Ca substitution, the surface-related contribution increases to 18%, 20%, and 52%, respectively. It is noteworthy that the contribution of the pseudocapacitive mechanism in PIBs is lower with respect to what is calculated for the same materials in LIBs and SIBs. Only the contribution of the pseudocapacitive process in $Ca_{1.5}V_2(PO_4)_3$/C material is more than 50%, while for the other three samples, it is less than 20%. Note that Na/K-ions are first inserted into the structure of $Li_{3-2x}Ca_xV_2(PO_4)_3$/C materials during the initial discharge process and then are de-inserted from the structure, which is different from both $Na_3V_2(PO_4)_3$ and $Na_3VCr(PO_4)_3$ cathodes that were first de-sodiation (charged) in the hybrid Mg-Na systems.[39] Another point is that the de-insertion of Li/Ca from the pristine $Li_{3-2x}Ca_xV_2(PO_4)_3$/C structure requires a high potential as that of cathodes. However, we cannot completely rule out the dual-cation (de)insertion in the current stages, which requires more effort to figure out and thus will be a follow-up work in the future.

4. Reaction Mechanism

In operando synchrotron diffraction was carried out to clarify the reaction mechanism of $Li_{3-2x}Ca_xV_2(PO_4)_3$/C during the discharge/charge process in SIBs due to their higher capacities compared with what is obtained in PIBs. **Figure 7** shows the two extreme cases of LVP and $Ca_{1.5}V_2(PO_4)_3$. At the beginning of the 1st sodiation process, most reflections of LVP keep their positions unchanged with a minor intensity decrease, and those reflections

 © 2023 The Authors. Small published by Wiley-VCH GmbH

16136829, 0, Downloaded from https://onlinelibrary.wiley.com/doi/10.1002/smll.202304102 by Karlsruher Inst F. Technologie, Wiley Online Library on [17/07/2023]. See the Terms and Conditions (https://onlinelibrary.wiley.com/terms-and-conditions) on Wiley Online Library for rules of use; OA articles are governed by the applicable Creative Commons License

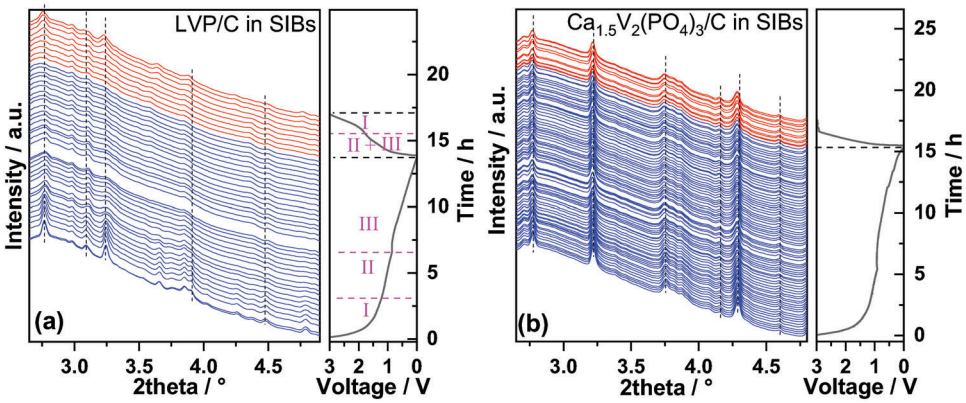

Figure 7. a) *In operando* synchrotron diffraction patterns of LVP/C and b) $Ca_{1.5}V_2(PO_4)_3$/C for the first cycle in Na-based electrolyte.

at 2.76° and 4.48° slightly shift to higher angles, indicating a solid solution process upon sodiation (Region I). with further Na^+ insertion (Region II), some reflections at 3.66°, 4.26°, and 4.79° gradually disappear while some new broad reflections at 2.78°, 3.12°, 3.27° appear and grow up, implying a two-phase transition process in this region. In region III, the reflections keep their positions unchanged with intensity decrease, which is caused by the formation of SEI on the electrode. Upon desodiation, the diffraction shows a reversible behavior. All reflections first keep their positions unchanged, followed by a very short two-phase reaction (Region III+II) and finally, a solid solution reaction (Region I). Note that when the electrode is charged to 3.0 V, these reflections almost return back to the original positions of pristine LVP with lower intensities, suggesting a partially irreversible structure change during the first cycle.

In contrast, all reflections of $Ca_{1.5}V_2(PO_4)_3$/C material, such as at 2.77° 3.22°, 3.75°, 4.16°, 4.29°, and 4.60°, gradually move toward lower 2θ angles with their intensities decreasing during the 1st sodiation process (Figure 7b), implying the solid solution process upon Na^+ insertion. At the same time, the diffraction evolution during the desodiation process suggests a reversible reaction. In brief, the reflections gradually move back to higher 2θ angles, but do not return back to their original positions, indicating that $Ca_{1.5}V_2(PO_4)_3$/C undergoes partial irreversibility during the first cycle. Interestingly, this is similar to the solid solution reaction of $Mg_3V_4(PO_4)_6$/carbon in both SIBs and PIBs, while $Mg_3V_4(PO_4)_6$/carbon goes through an indirect conversion reaction with the formation of Mg^0, V^0, and Li_3PO_4 in LIBs.

In order to probe the local electronic structure and environment of the active materials, *in operando* XAS was carried out on pure LVP/C and fully substituted $Ca_{1.5}V_2(PO_4)_3$/C in SIBs. **Figure 8** displays the normalized V K-edge X-ray absorption near-edge structure (XANES) spectra collected during the 1st cycle in SIBs. From OCV to 0.87 V, the edge position of the V K-edge for LVP gradually moves to lower energy. The pre-peak (A in Figure 8a) also moves toward lower energy with a decrease in intensity, implying the reduction of V during sodiation. The weak pre-edge peak on the XANES spectra of pristine LVP is due to the transitions between the 1s and bound p-hybridized d-states.[40] The edge resonance (B in Figure 8a, Supporting Information) that is related to the energy absorption by core electrons does not obviously change in both intensity and shape. With further decreasing the potential from 0.87 V to 0.01 V, the edge position only shows slight shifts to lower energy, which is attributed to the SEI formation. During the desodiation process, the edge position of V moves to higher energy and cannot return back to its original position (Figure 8b), implying the oxidation of V and partial irreversibility.

From OCV to 0.89 V, the edge position of the V K-edge for $Ca_{1.5}V_2(PO_4)_3$/C also slowly shifts to lower energy. The pre-peak (A in Figure 8c) also moves toward lower energy with a decrease in intensity, implying the reduction of V during sodiation. The edge resonance (B in Figure 8c) exhibits no obvious changes in both intensity and shape, too. With further decreasing the potential from 0.89 V to 0.01 V, the edge position shifts to lower energy and the intensity of the pre-peak shows a slight decrease, suggesting that the capacity at a low potential is not ascribed to the Na^+ insertion into the host material $Ca_{1.5}V_2(PO_4)_3$. Similarly, the edge position of V moves to higher energy and cannot return back to its original position (Figure 8d) during the desodiation process, suggesting the oxidation of V and partial irreversibility.

5. Conclusion

In this work, we extended the study of monoclinic LVP and Ca-substituted LVP as negative electrode materials for SIBs and PIBs and investigated the electrochemical properties of $Li_{3-2x}Ca_xV_2(PO_4)_3$/C (x = 0, 0.5, 1, and 1.5). Cyclic voltammetry demonstrates that one pair of broad peaks between 1.2 and 1.8 V can be observed for all samples in SIBs, while no clear peaks can be observed in PIBs. All samples in SIBs and PIBs proceed with a mixed contribution of diffusion-controlled and pseudocapacitive-type processes. Furthermore, the contribution of the pseudocapacitive process increases along with the increase of Ca content, where $Ca_{1.5}V_2(PO_4)_3$/C is based on the pseudocapacitive mechanism in both SIBs and PIBs. LVP/C shows the highest reversible capacity in SIBs and PIBs, while $Ca_{1.5}V_2(PO_4)_3$/C displays the best rate performance, with a capacity retention of 46% at 20 C in SIBs and a capacity retention of 47% at 10 C in PIBs. This study demonstrates that the specific capacity of SIBs and PIBs does not increase with the Ca-content as observed in LIBs, but the stability and performance at high C-rates can be improved by replacing Li^+ with Ca^{2+}. This implies that different cations insertion can strongly influence the redox

 © 2023 The Authors. Small published by Wiley-VCH GmbH

16136829, 0, Downloaded from https://onlinelibrary.wiley.com/doi/10.1002/smll.202304102 by Karlsruher Inst F. Technologie, Wiley Online Library on [17/07/2023]. See the Terms and Conditions (https://onlinelibrary.wiley.com/terms-and-conditions) on Wiley Online Library for rules of use; OA articles are governed by the applicable Creative Commons License

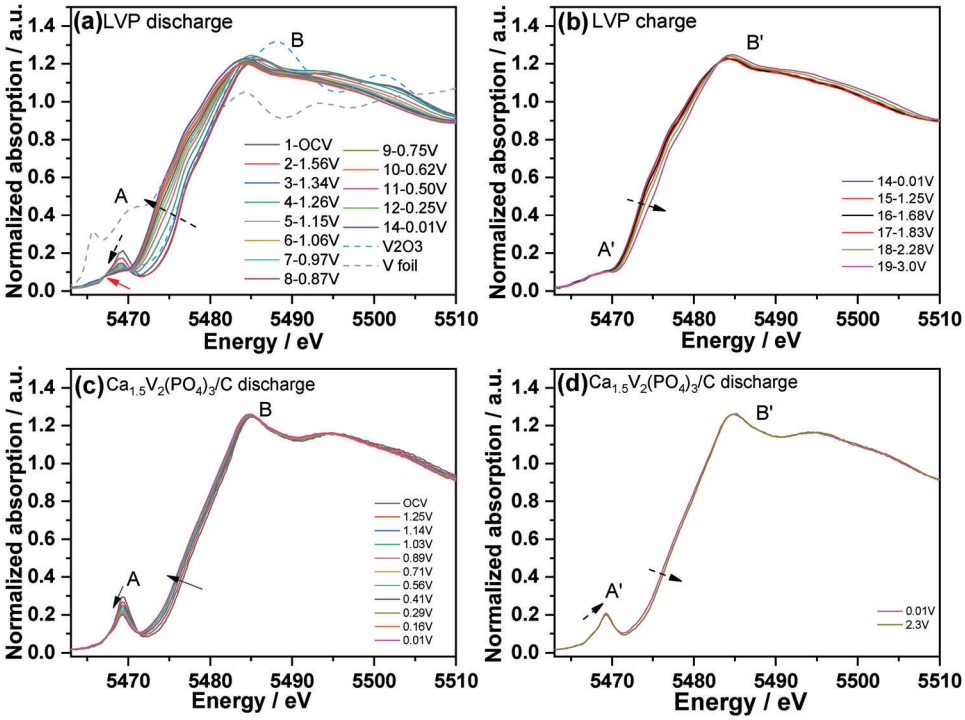

Figure 8. a,b) *In operando* V K-edge XANES spectra of LVP and c,d) $Ca_{1.5}V_2(PO_4)_3$ during the 1st cycle in Na-based electrolyte.

reaction and structure evolution of the host materials, which are related to the larger ion size of Na^+ and K^+ and their kinetics properties. Furthermore, *in operando* synchrotron diffraction and *in operando* X-ray absorption spectroscopy (XAS) elucidate the working mechanism of both LVP/C and $Ca_{1.5}V_2(PO_4)_3$/C in SIBs. The results demonstrate that LVP/C experiences a two-phase transition with partially irreversible structure change in SIBs while $Ca_{1.5}V_2(PO_4)_3$/C only undergoes solid solution reaction with partially irreversible structure change in SIBs.

Supporting Information

Supporting Information is available from the Wiley Online Library or from the author.

Acknowledgements

This work contributes to the research performed at CELEST (Center for Electrochemical Energy Storage Ulm-Karlsruhe) and was funded by the German Research Foundation (DFG) under Project ID 390874152 (POLiS Cluster of Excellence). This research work has gained benefit from beamtime allocation (2020094535-qfu) at BL04 – MSPD at ALBA Synchrotron, Barcelona, Spain. The authors acknowledge DESY (Hamburg, Germany), a member of the Helmholtz Association HGF, for the provision of experimental facilities. Parts of this research were carried out at PETRA III beamlines P02.1 and P64. Beamtime was allocated for proposal(s) I-20210736 and I-20200558. The *in operando* XAS work was performed by using the Biologic potentiostat of PETRA-III beamline P02.1. The authors thank Volodymyr Baran and Akhil Tayal from DESY for their technical support during measurements. Kristina Pfeifer (IAM-ESS) and Liuda Mereacre are gratefully acknowledged for SEM and TGA measurements, respectively.

Open access funding enabled and organized by Projekt DEAL.

Conflict of Interest

The authors declare no conflict of interest.

Data Availability Statement

The data that support the findings of this study are available from the corresponding author upon reasonable request. The orginal data are available at KITOpen through the DOI:10.35097/1443.

Keywords

electrochemical performance, monoclinic $Li_3V_2(PO_4)_3$, negative electrode materials, potassium-ion batteries, sodium-ion batteries

Received: May 16, 2023
Revised: June 14, 2023
Published online:

[1] a) Y. Hamon, T. Brousse, F. Jousse, P. Topart, P. Buvat, D. M. Schleich, *J. Power Sources* **2001**, *97–98*, 185; b) M. N. Obrovac, V. L. Chevrier, *Chem. Rev.* **2014**, *114*, 11444.
[2] a) M. Okoshi, Y. Yamada, S. Komaba, A. Yamada, H. Nakai, *J. Electrochem. Soc.* **2017**, *164*, A54; b) D. Stępień, Z. Zhao, S. Dsoke, *J. Electrochem. Soc.* **2018**, *165*, A2807.
[3] K. Kubota, M. Dahbi, T. Hosaka, S. Kumakura, S. Komaba, *Chem. Rec.* **2018**, *18*, 459.
[4] N. Yabuuchi, K. Kubota, M. Dahbi, S. Komaba, *Chem. Rev.* **2014**, *114*, 11636.
[5] N. Leifer, M. F. Greenstein, A. Mor, D. Aurbach, G. Goobes, *J. Phys. Chem. C* **2018**, *122*, 21172.

 © 2023 The Authors. Small published by Wiley-VCH GmbH

16136829, 0, Downloaded from https://onlinelibrary.wiley.com/doi/10.1002/smll.202304102 by Karlsruher Inst F. Technologie, Wiley Online Library on [17/07/2023]. See the Terms and Conditions (https://onlinelibrary.wiley.com/terms-and-conditions) on Wiley Online Library for rules of use; OA articles are governed by the applicable Creative Commons License

[6] K. Nobuhara, H. Nakayama, M. Nose, S. Nakanishi, H. Iba, *J. Power Sources* **2013**, *243*, 585.
[7] Z. L. Jian, W. Luo, X. L. Ji, *J. Am. Chem. Soc.* **2015**, *137*, 11566.
[8] J. Y. Hwang, S. T. Myung, Y. K. Sun, *Adv. Funct. Mater.* **2018**, *28*, 1802938.
[9] L.-F. Zhao, Z. Hu, W.-H. Lai, Y. Tao, J. Peng, Z.-C. Miao, Y.-X. Wang, S.-L. Chou, H.-K. Liu, S.-X. Dou, *Adv. Energy Mater.* **2021**, *11*, 2002704.
[10] a) Z. Jian, S. Hwang, Z. Li, A. S. Hernandez, X. Wang, Z. Xing, D. Su, X. Ji, *Adv. Funct. Mater.* **2017**, *27*, 1700324; b) Z. Li, L. Ma, T. W. Surta, C. Bommier, Z. Jian, Z. Xing, W. F. Stickle, M. Dolgos, K. Amine, J. Lu, T. Wu, X. Ji, *ACS Energy Lett.* **2016**, *1*, 395.
[11] https://www.catl.com/en/news/665.html.
[12] X. Rui, Q. Yan, M. Skyllas-Kazacos, T. M. Lim, *J. Power Sources* **2014**, *258*, 19.
[13] R. Satish, V. Aravindan, W. C. Ling, S. Madhavi, *J. Power Sources* **2015**, *281*, 310.
[14] a) Q. Fu, S. Liu, A. Sarapulova, L. Zhu, M. Etter, E. Welter, P. G. Weidler, M. Knapp, H. Ehrenberg, S. Dsoke, *Adv. Energy Mater.* **2019**, *9*, 1901864; b) Q. Ni, L. Zheng, Y. Bai, T. Liu, H. Ren, H. Xu, C. Wu, J. Lu, *ACS Energy Lett.* **2020**, *5*, 1763.
[15] T. Akçay, M. Häringer, K. Pfeifer, J. Anhalt, J. R. Binder, S. Dsoke, D. Kramer, R. Mönig, *ACS Appl. Energy Mater.* **2021**, *4*, 12688.
[16] D. Wang, N. Chen, M. Li, C. Wang, H. Ehrenberg, X. Bie, Y. Wei, G. Chen, F. Du, *J. Mater. Chem. A* **2015**, *3*, 8636.
[17] L. Zhang, B. W. Zhang, C. R. Wang, Y. H. Dou, Q. Zhang, Y. J. Liu, H. Gao, M. Al-Mamun, W. K. Pang, Z. P. Guo, S. X. Dou, H. K. Liu, *Nano Energy* **2019**, *60*, 432.
[18] Q. Fu, B. Schwarz, Z. Ding, A. Sarapulova, P. G. Weidler, A. Missyul, M. Etter, E. Welter, W. Hua, M. Knapp, S. Dsoke, H. Ehrenberg, *Adv. Sci.* **2023**, *10*, 2207283.
[19] M. Herklotz, F. Scheiba, M. Hinterstein, K. Nikolowski, M. Knapp, A.-C. Dippel, L. Giebeler, J. Eckert, H. Ehrenberg, *J. Appl. Crystallogr.* **2013**, *46*, 1117.
[20] J. Rodríguez-Carvajal, *in Commission on Powder Diffraction (IUCr)*, *Newsletter* Vol. *26*, **2001**, p. 12.
[21] S. Brunauer, P. H. Emmett, E. Teller, *J. Am. Chem. Soc.* **1938**, *60*, 309.
[22] a) in *Adsorption by Powders and Porous Solids*, (Eds: F. Rouquerol, J. Rouquerol, K. Sing), Academic Press, London, **1999**, p. 460; b) M. Thommes, B. Smarsly, M. Groenewolt, P. I. Ravikovitch, A. V. Neimark, *Langmuir* **2006**, *22*, 756; c) M. Thommes, K. Kaneko, V. Neimark Alexander, P. Olivier James, F. Rodriguez-Reinoso, J. Rouquerol, S. W. Sing Kenneth, *Pure Appl. Chem.* **2015**, *87*, 1051.
[23] J. Landers, G. Y. Gor, A. V. Neimark, *Colloids Surf. A* **2013**, *437*, 3.
[24] F. Fauth, I. Peral, C. Popescu, M. Knapp, *Powder Diffr.* **2013**, *28*, S360.
[25] J. Filik, A. W. Ashton, P. C. Y. Chang, P. A. Chater, S. J. Day, M. Drakopoulos, M. W. Gerring, M. L. Hart, O. V. Magdysyuk, S. Michalik, A. Smith, C. C. Tang, N. J. Terrill, M. T. Wharmby, H. Wilhelm, *J. Appl. Crystallogr.* **2017**, *50*, 959.
[26] B. Ravel, M. Newville, *J. Synchrotron Radiation* **2005**, *12*, 537.
[27] V. V. Kravchenko, V. I. Michailov, S. E. Sigaryov, *Solid State Ionics* **1992**, *50*, 19.
[28] Z. Jian, Y. Sun, X. Ji, *Chem. Commun.* **2015**, *51*, 6381.
[29] a) J. Deng, W.-B. Luo, S.-L. Chou, H.-K. Liu, S.-X. Dou, *Adv. Energy Mater.* **2018**, *8*, 1701428; b) H. Kim, H. Kim, Z. Ding, M. H. Lee, K. Lim, G. Yoon, K. Kang, *Adv. Energy Mater.* **2016**, *6*, 1600943; c) M. A. Munoz-Marquez, D. Saurel, J. L. Gomez-Camer, M. Casas-Cabanas, E. Castillo-Martinez, T. Rojo, *Adv. Energy Mater.* **2017**, *7*, 1700463; d) H. Hou, L. Shao, Y. Zhang, G. Zou, J. Chen, X. Ji, *Adv. Sci.* **2017**, *4*, 1600243; e) R. Dong, L. Zheng, Y. Bai, Q. Ni, Y. Li, F. Wu, H. Ren, C. Wu, *Adv. Mater.* **2021**, *33*, 2008810.
[30] a) Y. Xu, Q. Wei, C. Xu, Q. Li, Q. An, P. Zhang, J. Sheng, L. Zhou, L. Mai, *Adv. Energy Mater.* **2016**, *6*, 1600389; b) R. Klee, M. J. Aragón, P. Lavela, R. Alcántara, J. L. Tirado, *ACS Appl. Mater. Interfaces* **2016**, *8*, 23151.
[31] Q. Zhu, M. Wang, B. Nan, H. Shi, X. Zhang, Y. Deng, L. Wang, Q. Chen, Z. Lu, *J. Power Sources* **2017**, *362*, 147.
[32] T. Brousse, D. Bélanger, J. W. Long, *J. Electrochem. Soc.* **2015**, *162*, A5185.
[33] S. Ardizzone, G. Fregonara, S. Trasatti, *Electrochim. Acta* **1990**, *35*, 263.
[34] G. A. Muller, J. B. Cook, H.-S. Kim, S. H. Tolbert, B. Dunn, *Nano Lett.* **2015**, *15*, 1911.
[35] a) J. Han, Y. Niu, S.-j. Bao, Y.-N. Yu, S.-Y. Lu, M. Xu, *Chem. Commun.* **2016**, *52*, 11661; b) J. Han, M. Xu, Y. Niu, G.-N. Li, M. Wang, Y. Zhang, M. Jia, C. m. Li, *Chem. Commun.* **2016**, *52*, 11274; c) B. Kishore, G. Venkatesh, N. Munichandraiah, *J. Electrochem. Soc.* **2016**, *163*, A2551; d) L. Zhang, B. Zhang, C. Wang, Y. Dou, Q. Zhang, Y. Liu, H. Gao, M. Al-Mamun, W. K. Pang, Z. Guo, S. X. Dou, H. K. Liu, *Nano Energy* **2019**, *60*, 432.
[36] L. Li, S. Zhao, Z. Hu, S.-L. Chou, J. Chen, *Chem. Sci.* **2021**, *12*, 2345.
[37] a) L. Fan, R. Ma, Q. Zhang, X. Jia, B. Lu, *Angew. Chem., Int. Ed.* **2019**, *58*, 10500; b) H. Wang, D. Yu, X. Wang, Z. Niu, M. Chen, L. Cheng, W. Zhou, L. Guo, *Angew. Chem., Int. Ed.* **2019**, *58*, 16451; c) J. Zhao, X. X. Zou, Y. J. Zhu, Y. H. Xu, C. S. Wang, *Adv. Funct. Mater.* **2016**, *26*, 8103.
[38] Q. Fu, H. Zhao, A. Sarapulova, S. Dsoke, *Appl. Res.* **2022**, *2*, e202200070.
[39] a) S. Rubio, R. Liu, X. Liu, P. Lavela, J. L. Tirado, Q. Li, Z. Liang, G. F. Ortiz, Y. Yang, *J. Mater. Chem. A* **2019**, *7*, 18081; b) M. Cabello, R. Alcantara, F. Nacimiento, P. Lavela, M. J. Aragon, J. L. Tirado, *Electrochim. Acta* **2017**, *246*, 908.
[40] J. Wong, F. W. Lytle, R. P. Messmer, D. H. Maylotte, *Phys. Rev. B* **1984**, *30*, 5596.

 © 2023 The Authors. Small published by Wiley-VCH GmbH

16136829, 0, Downloaded from https://onlinelibrary.wiley.com/doi/10.1002/smll.202304102 by Karlsruher Inst F. Technologie, Wiley Online Library on [17/07/2023]. See the Terms and Conditions (https://onlinelibrary.wiley.com/terms-and-conditions) on Wiley Online Library for rules of use; OA articles are governed by the applicable Creative Commons License